Functionalization of Scanning Probe Tips with Epitaxial Semiconductor Layers

Valeria Giliberti, Emilie Sakat, Monica Bollani, M. Virginia Altoe, Mauro Melli, Alexander Weber-Bargioni, Leonetta Baldassarre, Michele Celebrano, Jacopo Frigerio, Giovanni Isella, Stefano Cabrini, and Michele Ortolani*

Functionalized scanning probe tips hold great promise for the controlled delivery of signals from and to selected nanoscale volumes. Here, a new nanotechnological approach for the functionalization of scanning probe tips is presented, targeting the transfer of the optical, electrical, thermal, or chemical properties of precisely characterized epitaxial semiconductor layers to the nanoscale probe tip. Homogeneously doped, strain-relaxed hetero-epitaxial germanium layers, several micrometers thick, are first grown on silicon wafers by low-energy plasma-enhanced chemical vapor deposition and then employed to functionalize the probe apex. This choice of materials and growth technique enables the future scalability of the tip functionalization process toward high production volumes. The fabricated probe tips are investigated in a transmission electron microscope, revealing that the crystal structure and the homogeneous doping level of the epitaxial layers are unchanged after the probe-tip functionalization process. These doped-germanium tips are also tested as nanoemitters of light at telecom wavelengths (1.55 μm) and applied as scattering probes for near-field mid-infrared microscopy. The reported combination of heteroepitaxial growth and a nanofabrication approach can be extended to a variety of epitaxial materials, thus enabling a new generation of scanning probes for the investigation of nanostructured materials and devices.

1. Introduction

Functionalization of scanning probe tips makes it possible to access specific material properties combined with imaging at the nanoscale.[1] The constituent material of the probe tip is deemed unessential to the mechanical feedback loops that stand behind the technology for topography imaging performed by atomic force microscopy (AFM), whose lateral resolution only depends on the tip geometry. Using functionalized scanning probe tips with peculiar optical, chemical, or electrical properties, it has been demonstrated that the interaction volume of analytical methods such as spectroscopy[2–5] fluorescence imaging,[6,7] thermal conductance mapping,[8] or electrochemical potential mapping[9–11] can be reduced by many orders of magnitude. Following this path, these well-established analytical methods could then be brought to the nanoscale for routine analyses of nanomaterials. In this context, different advanced strategies for tip functionalization have been

Dr. V. Giliberti, Dr. L. Baldassarre, Dr. M. Ortolani
Dipartimento di Fisica
Sapienza Università di Roma
Piazzale Aldo Moro 5, I-00185 Roma, Italy
E-mail: michele.ortolani@roma1.infn.it

Dr. V. Giliberti, Dr. L. Baldassarre
Istituto Italiano di Tecnologia
Center for Life NanoSciences
Viale Regine Elena 291, I-00161 Roma, Italy

Dr. E. Sakat, Dr. M. Celebrano, Dr. J. Frigerio, Prof. G. Isella
Dipartimento di Fisica
Politecnico di Milano
Piazza Leonardo da Vinci, 32, I-20133 Milan, Italy

Dr. E. Sakat
Laboratoire Charles Fabry
Institut d'Optique Graduate School
CNRS
Université Paris-Saclay
91127 Palaiseau, France

Dr. M. Bollani, Prof. G. Isella, Dr. M. Ortolani
Istituto di Fotonica e Nanotecnologie
Consiglio Nazionale delle Ricerche (IFN-CNR)
Piazza Leonardo da Vinci, 32, I-20133 Milano, Italy

Dr. M. Bollani, Dr. J. Frigerio, Prof. G. Isella
L-NESS
Dipartimento di Fisica del Politecnico di Milano
Polo di Como
Via Anzani 42, I-22100 Como, Italy

Dr. M. V. Altoe, Dr. M. Melli, Dr. A. Weber-Bargioni, Dr. S. Cabrini
Molecular Foundry
Lawrence Berkeley National Laboratories
1 Cyclotron Road, Berkeley, CA 94720, USA

small
methods
www.small-methods.com

ADVANCED
SCIENCE NEWS
www.advancedsciencenews.com

adopted and they can be coarsely divided into: i) coating of the surface of existing tips with metals,[12] dielectrics,[13] molecules,[14,15] nanocrystals,[16] or quantum dots;[17,18] ii) attachment of pre-existing functional nano-objects such as metal nanowires,[19,20] carbon nanotubes,[21] or fluorescent particles;[17,22] iii) nanofabrication of structures on the tip itself, including fluidic channels for liquid electrodes,[23] optical nanoantennas for spectroscopy,[4,24–27] and electrical contacts.[28] The direct fabrication of scanning probe tips out of functional bulk materials different from inert silicon or glass has seldom been reported,[29] although this strategy would clearly provide the advantage of a probe with precisely precharacterized material properties. This work is focused on the functionalization of scanning probe tips with epitaxial semiconductor materials, with the aim of transferring the material functionalities to the nanoscale. Before being transferred to the nanoscale probe, the material properties are precharacterized on large-area films obtained with reproducible epitaxial material growth techniques. Detailed structural, chemical, and morphological analyses performed at the nanoscale on the functionalized probe tips after the transfer process demonstrate that our approach preserves the high crystal quality and the tailored optical and electrical properties of the epitaxial layers, which indeed derive from the crystalline structure of the epilayers. To demonstrate the validity of our concept, we have grown epitaxial heavily doped germanium films on silicon wafers and we have fabricated several scanning probes out of them. The unique optical properties of doped-Ge in the infrared (IR) range, which cannot be obtained in standard doped-Si AFM probe tips, include photoluminescence emission at the telecom wavelength of 1.55 µm and a small effective mass of electrons resulting in very high plasma frequencies in the mid-IR (i.e., the highest electromagnetic frequency at which the free carriers can screen the radiation electric field).[30] In this work, the optical functionalities of these probes are experimentally demonstrated to be in agreement with the predictions based on the crystal structure, doping level, and on-wafer characterization of the as-grown Ge films. To further corroborate our findings, we illustrate two possible scanning probe microscopy applications of these functionalized tips for the characterization of nanophotonic circuits and nanomaterials. It is worth noticing that, conversely to other epitaxial materials, our epitaxial layers grown on silicon wafers allow envisioning future production of functionalized probe tips that could be up-scaled to large volumes by partial modification of the fabrication process of silicon cantilever probe chips for AFM.

2. Fabrication of Scanning Probe Tips from the Epitaxial Germanium Film

In order to simplify the first demonstration of our functionalization process, we decided to start from epitaxial films with thickness of several micrometers and homogeneous doping level, which give us maximum fabrication tolerance on the final pyramidal shape of the probe tips. To this aim, heteroepitaxial Ge films were grown on Si wafers by low-energy plasma-enhanced chemical vapor deposition (LEPECVD). LEPECVD is a versatile variant of conventional CVD techniques,

in which the use of the plasma parameters to enhance the deposition efficiency allows independent optimization of the growth rate (controlled by the plasma density) and of the mobility of the adatoms (controlled by the substrate temperature).[31] In this way, the main material science issue of Ge-on-Si epitaxy, which is the 4% larger lattice parameter of Ge if compared to Si,[32–34] is circumvented by performing out-of-equilibrium growth of relatively thick strain-relaxed heteroepitaxial Ge layers.[35,36] Strain-relaxed, heavily electron-doped germanium (n-Ge) films several micrometers thick (2–4 µm), are first grown have been grown on industrial-grade Si substrates along the [001] crystal axis of Ge and Si by introducing simultaneously germane (GeH_4) and phosphine (PH_3) in the LEPECVD growth reactor, in order to incorporate P as a donor in the Ge crystal lattice. By varying the PH_3/GeH_4 ratio, activated doping levels comprised between $n \approx 0.35$–3.6×10^{19} cm^{-3} have been achieved.

In **Figure 1**a, we schematically illustrate the concept idea of probe tip functionalization and in Figure 1b, the scanning electron microscopy (SEM) images of some representative probe tips exhibiting different pyramidal shapes are shown. The novel probe design consists in a standard AFM chip, with mechanical properties of the silicon cantilever suited for the final application, where the original tip apex has been removed and the new tip apex is functionalized with the target epitaxial semiconductor material. The transfer of the epitaxial layers from the growth wafers to a scanning probe is done through several steps of top-down 3D nanofabrication technology.[37] In a preliminary process step, a dense pattern of micropillars with aspect ratio of about 6 is etched into the epitaxial wafers. Also, the tip of commercial AFM visible-apex probes is truncated by focused ion beam (FIB) milling with Ga ions. Subsequently, by using a piezoelectric nanomanipulator installed into the FIB/SEM chamber where the patterned epitaxial wafer is located, one of the AFM probe chips with truncated tip apex is put in contact with the top surface of one of the micropillars (Figure 1c, subpanels 1,2). The truncated tip and the micropillar are glued together by electron beam-induced deposition (EB-ID) of a carbon–platinum alloy (Figure 1c, subpanel 3). The mechanical extraction of the epitaxial material from the Si substrate is then performed by FIB milling of the micropillar base at high Ga ion current (Figure 1c, subpanel 4) and elastic release with the AFM cantilever (Figure 1c, subpanels 5,6). The final pyramidal shapes of the functionalized tips (some of them in Figure 1b) are then obtained by finely tuned FIB milling at low Ga ion current in order to minimize the damage of the epitaxial material and obtain a sharp tip apex. AFM topography imaging in contact mode of cleaved mica surfaces, used as test samples, is finally performed with the functionalized tips to verify their mechanical stability. In Figure 1d, we report the AFM topography maps of cleaved mica surfaces obtained with one of the tips. The obtained test sample morphology is comparable to that obtained by commercial scanning probe tips. We also note that the observed performance of the functionalized tips was rather standard for tapping-mode AFM imaging, i.e., several days of continuous operation on solid-state samples with height variation of 100–500 nm, as we tested in the scanning probe microscopy experiment described later on.
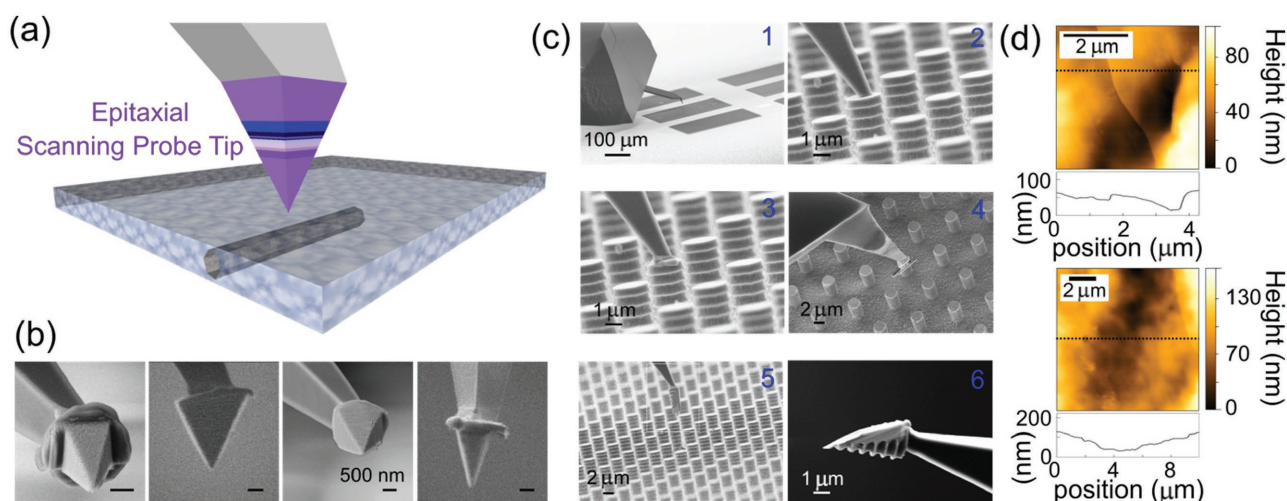
ADVANCED
SCIENCE NEWS
www.advancedsciencenews.com

small
methods
www.small-methods.com

FULL PAPER

Figure 1. a) Concept of the scanning probe tips functionalized with epitaxial materials in order to transfer their optical functions to the tip for investigation of samples at the nanoscale. b) SEM images of four different functionalized scanning probe tips fabricated out of epitaxial heavily doped Ge-on-Si. The size of the scale bar is 500 nm for all four SEM images (note the slightly different length of the bar in each panel). c) The subpanels from (1) to (6) illustrate the subsequent steps of the scanning probe functionalization process, which consists in the transfer of the epitaxial layers from the growth substrate, previously patterned into arrays of cylindrical micropillars, to an AFM probe chip with truncated tip apex. d) AFM topography of two different regions of a cleaved mica surface performed in contact-mode with one of the functionalized tip for mechanical stability test. In the two plots below the maps, the AFM line scans indicated by the dotted black lines are reported.

3. Nanostructural Characterization of the Functionalized Tips

In order to determine the structural properties and the chemical composition of the functionalized tips, some of them were mounted after the functionalization process in a high-resolution transmission electron microscope (TEM). In **Figure 2**a–c, bright-field TEM images of one of the n-Ge probes are reported for three different magnification values. The first two images show the smooth diagonal walls of the pyramid tip with clearly defined angle and radius of curvature $R \approx 75$ nm. The external material layer appears to have become amorphous probably due to the high energy of the processes involved in FIB milling with Ga ions. The high-magnification high-angle annular dark-field (HAADF) images taken with different angle of incidence and reported in Figure 2d–g reveal that the amorphous layer coats almost the entire tip surface, down to around 50 nm depth.

In order to gain information on the crystal structure in the interior of the pyramid, we performed nanobeam electron diffraction in several spots containing different ratios of bulk and surface Ge atoms. By looking at Figure 2i, it is evident that von Laue circles are detected in the diffraction pattern when the TEM spot is positioned at the very apex of the tip (blue circle in the TEM image in Figure 2h, probing Ge atoms belonging to the surface layer). This confirms the amorphous nature of the surface layer. Instead, clear evidence of a Bragg lattice is found in Figure 2j,k when the nanobeam is directed into the pyramid body by only 50 nm below the surface (red circle in Figure 2h, probing a much higher fraction of bulk Ge atoms), indicating that the epitaxial crystal structure is preserved in the interior of the tip. The diffraction spots seen in Figure 2k belong to a 2D pattern of Bragg peaks very close to that expected for the {012} plane of Ge. The reciprocal space lattice parameters correspond to the values predicted for the cubic lattice of Ge. Also,

one clearly sees that the crystallographic direction (001) is oriented along the pyramid axis, as expected since it corresponds to the epitaxial growth axis. In summary, the structural studies presented here indicate that the high crystal quality of epitaxial layers is preserved throughout the probe fabrication steps when the epitaxial layers are nanosculptured in the shape of a pyramid by FIB.

The elemental composition of the tip at the nanoscale was determined by X-ray energy-dispersive spectroscopy (EDS) for each point where the electron beam was focused while scanning the entire probe tip (**Figure 3**a), with the aim of quantifying the Ga ion implantation which may have taken place during the FIB milling process. This is especially important for n-Ge, because Ga acts as an electron acceptor in the Ge lattice, therefore the implantation of Ga ions could severely affect the heavy electron-doping levels obtained in the LEPECVD growth of n-Ge. Looking at the elemental density maps in Figure 3b–d, one sees that the tip is entirely made of Ge and that the material deposited by EB-ID to glue the tip to the Si cantilever is Pt, as expected. The total elemental composition is summarized in the X-ray EDS spectrum reported in Figure 3e. No clear peak at 9.2 keV related to the presence of Ga ions can be identified, demonstrating that major Ga contamination of the n-Ge tips can be excluded. When reducing the integration volume to the pyramid only, in specific cases weak imprints of Ga contamination were identified, as for the tip reported in Figure 3f–j. The Ga peak at 9.2 keV is indeed revealed in the high-resolution X-ray EDS spectrum in Figure 3j. As for the first tip, Pt is detected exclusively in the glue block, and Si exclusively in the tip shaft. However, in this case, the tip features detectable amount of Ga distributed over the entire pyramid (map not shown due to low signal-to-background ratio). An upper/lower limit to the total atomic concentration of gallium in the the probe tips deduced from X-ray EDS analysis is between 0.01% and 0.1% of the total
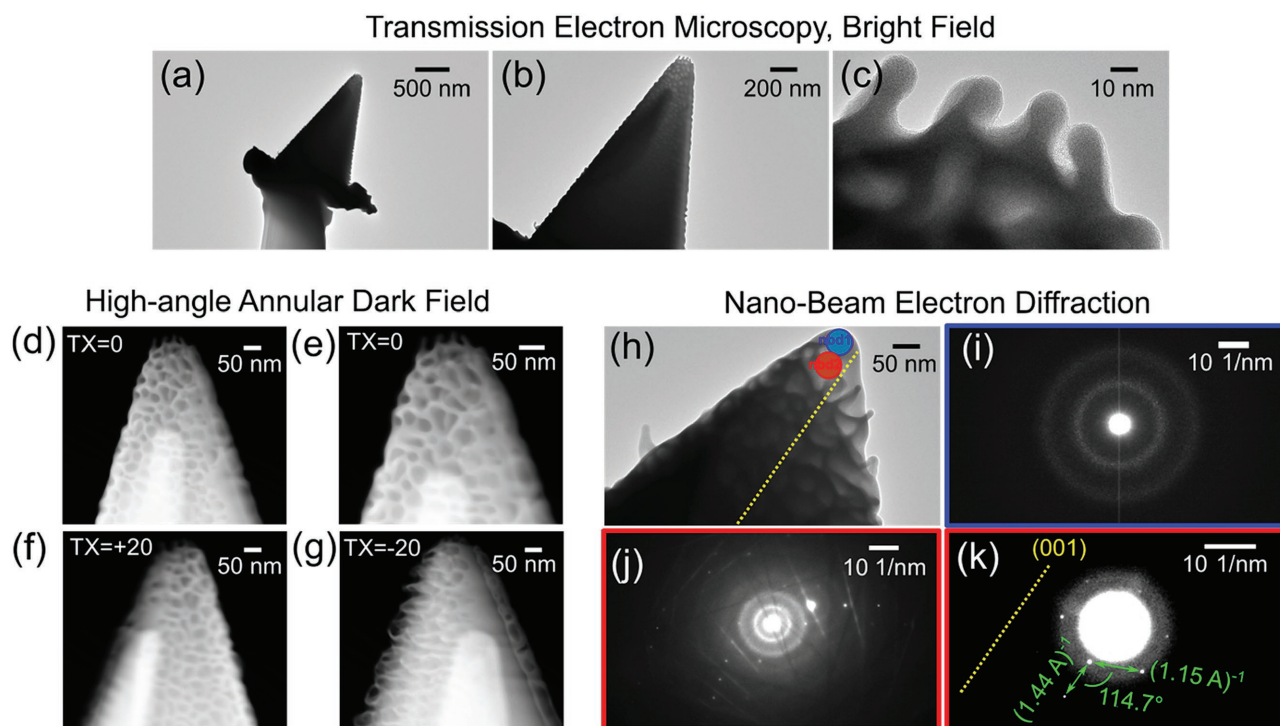
Transmission Electron Microscopy, Bright Field

High-angle Annular Dark Field

Nano-Beam Electron Diffraction

Figure 2. Structural analysis with nanoscale resolution of one of the fabricated tips performed by: a–c) bright-field TEM, d–g) HAADF-TEM, and h–k) nanobeam electron diffraction. Panels (a)–(c) are bright-field TEM images with increasing magnification. Panels (d)–(g) are HAADF-TEM images with different tilt angles along the horizontal direction TX, indicated in degrees. h) Bright-field TEM image with the two positions (blue, red) where nanobeam electron diffraction was performed. i) Diffraction pattern at the apex (blue circle in panel (h)): the presence of an amorphous structure is demonstrated by the von Laue circles. j) Diffraction pattern taken with the nanobeam 50 nm inside the tip (red circle in panel (h)): the crystalline structure is demonstrated by the Bragg spots and Kikuchi lines. k) Enlarged view of the center of the image in panel (j), from which reciprocal lattice parameters are extracted and found to be compatible with that of Ge, considering that the (001) axis runs parallel to the yellow dotted line, which is itself parallel to the growth axis and to the tip axis (yellow dotted line in panel (h)). The image contrast in panel (k) has been enhanced to highlight the position of the Bragg spots.

atomic concentration of Ge, which is compatible with strong surface contamination with 25 nm implantation depth typically found in semiconductors exposed to a 30 keV Ga ion beam, as the one employed for FIB fabrication. This level of contamination is not affecting the optical functionalities of the probes, as it will be demonstrated later on in this work.

4. Optical Properties of Epitaxial Germanium-on-Silicon

In this section we introduce the general optical properties of the epitaxial Ge-on-Si material to be transferred to the probe tip, then we describe two experiments where the n-Ge functionalized probe tips were used for scanning confocal photoluminescence (PL) microspectroscopy in the near-IR[38] and for aperture-less scattering-type scanning near-field optical microscopy (s-SNOM) in the mid-IR.[4,39] These two experiments highlight potential applications of the functionalized tips.

4.1. Near-Infrared Photoluminescence

The implementation of CVD epitaxial growth of Ge-on-Si as one of the standard steps of silicon foundry processes has the

potential to revolutionize optoelectronic technology. Ge-on-Si is already used in silicon photonics due to its IR detection and emission properties for the on-chip fabrication of radiation detectors at the standard telecom wavelength $\lambda = 1.55$ μm, which approximately coincides with the absorption edge of bulk strain-relaxed Ge.[40] These detectors can now even be integrated in the complementary metal oxide semiconductor (CMOS) process.[41] Recently, heteroepitaxial films of the direct-gap GeSn alloy grown by CVD on Ge-on-Si substrates have demonstrated laser action on a silicon wafer,[42] however at longer IR wavelengths $\lambda > 2$ μm. High electron-doping levels together with precise control of strain may be necessary to achieve laser gain at $\lambda = 1.55$ μm in pure Ge,[43,44] while nanocavities at 1.55 μm made of n-Ge have already been achieved.[38] The current need for on-chip characterization techniques for silicon photonics has partly motivated the development of the Ge-on-Si scanning probe tips presented in this work. Indeed, by acting as local IR emitters at $\lambda = 1.55$ μm, our functionalized probe tip could be used to test on-chip CMOS-integrated IR detectors, resonators, and waveguides.

As a first demonstration of the optical functionality of the epitaxial layers forming our scanning probe tips, we performed PL microspectroscopy recording spectra and spatial maps of the spontaneous emission of a n-Ge tip at the direct-gap energy $E_g = 0.80$ eV corresponding to an IR wavelength $\lambda \approx 1.55$ μm. Electromagnetic simulations and initial tests were previously
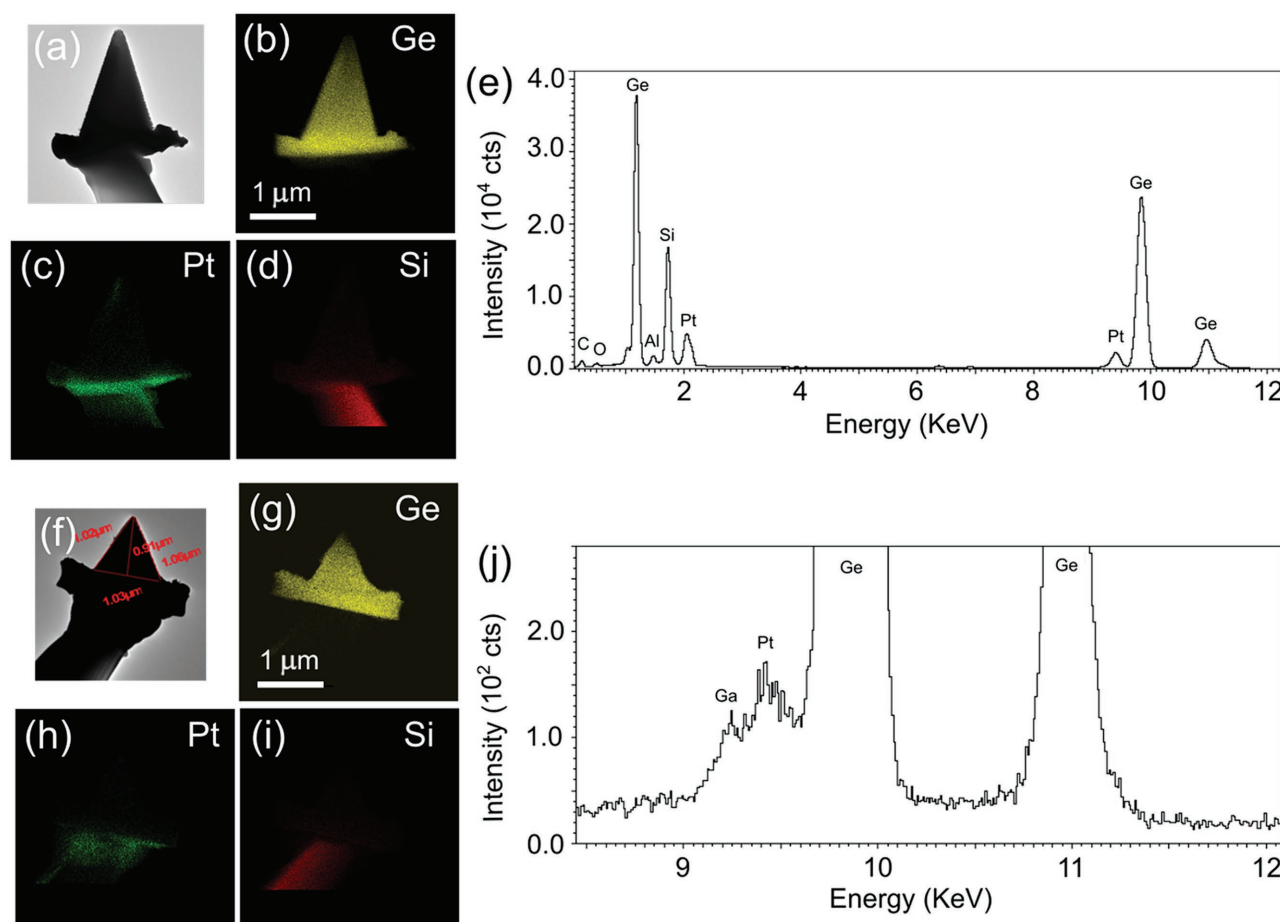
Figure 3. Composition analysis by X-ray EDS with nanoscale resolution on two of the fabricated tips. TEM image of the a) tip and local concentration of b) Ge, c) Pt, and d) Si in the tip. e) X-ray EDS spectrum integrated over the full TEM image of panel (a). The peak intensity at 9.8 keV is used to build the image in panel (b), while the peaks at 9.4 and 1.7 keV are used for panels (c) and (d), respectively. Note that the weak Al peak at 1.5 keV comes from the tip-holder and it is not contained in the functionalized probe. f–i) Same as panels (a)−(d) for a distinct functionalized probe tip. In panel (j), the X-ray EDS spectrum is integrated only over the pyramid. The smaller integration volume in the tip of panel (j) enabled the detection of Ga contamination in the tip (9.2 keV peak), which is probably due to implantation during the FIB milling process. Note that the donor concentration (phosphorous) is in the range of 0.1 at% and therefore it cannot be detected with the present X-ray EDS sensitivity.

carried out to determine how the micropyramid acts as an effective subwavelength-sized photon source.[45] We used a confocal microscopy setup with an excitation diode laser source emitting at 785 nm coupled to a high numerical aperture (N.A. = 0.9) air objective, which tightly focuses the laser beam on the tip (see sketch of the setup in **Figure 4**a). In Figure 4b, we report a typical diffraction-limited image of one of the tips mounted in the confocal microscope obtained by detecting the scattered light at 785 nm. In this case, the signal was recorded from both the n-Ge tip and from the silicon part of the probe. On the contrary, in the luminescence emission map obtained by selecting a spectral window around 1550 nm (Figure 4c), a much smaller area can be clearly identified in the image as the only source of the emitted signal. By moving the tip by 0.5 µm in both z directions outside the focal plane (z = ±0.5 µm), the signal collected at 1550 nm drops considerably, while the 785 nm scattering signal is still rather high. One can then safely identify the entire n-Ge tip body as the subwavelength volume emitting photons around 1550 nm under focused excitation at 785 nm. For

quantitative evaluation, we benchmark the tip PL data against those taken from a single Ge pillar on the original epilayer, which was not subject to any further fabrication process step. The PL spectra of the single pillar (red dashed curve) and that of the tip (blue curve), acquired with the same excitation powers, are reported in Figure 4d. The spectral shape of the emission is preserved within the available spectral resolution, and the emission intensity measured from the pillar actually exceeds that from the tip by a factor 4.5. According to our electromagnetic simulations, in which spontaneous emission is mimicked with a set of randomly positioned and randomly oriented incoherent emitting dipole,[38] this factor is compatible with the difference in emission volume weighted by the electromagnetic radiation from the emitting dipole, indicating that the emission rate per unit volume is preserved during the functionalization process. In perspective, our functionalized tips could operate as scanning nanoemitters of photons at the standard telecom wavelength λ = 1.55 µm for on-chip characterization of nanophotonic circuits.[46]

FULL PAPER

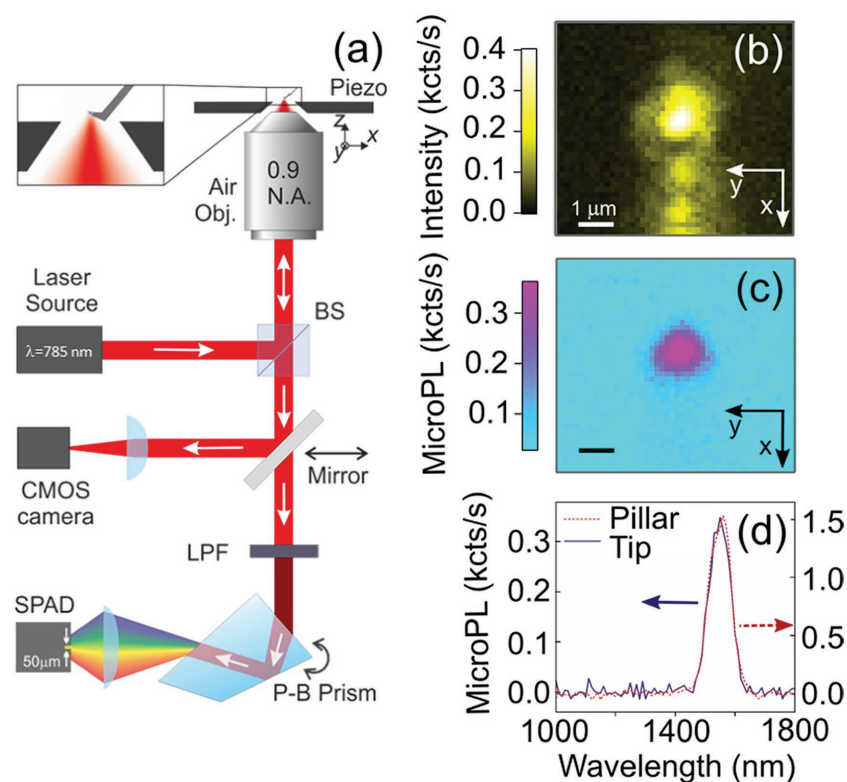**Figure 4.** PL confocal microscopy experiment demonstrating emission of photons in the spectral range λ = 1430–1650 nm. a) Confocal setup employed for the PL microspectroscopy experiment (BS: beamsplitter). In the first detection arm a CMOS camera is used for imaging at 785 nm. In the second detection arm, a single-photon avalanche photodetector (SPAD) is used after a long-pass filter (LPF) and a Pelin–Broca prism for spectral analysis of PL emission. b) Elastic scattering image at 785 nm. c) PL emission map at 1550 nm. d) Comparison between the PL spectrum of one of the micropillars before fabrication and that of the tip after fabrication.

4.2. Mid-Infrared Scattering-Type Near-Field Microscopy

The normal-incidence IR reflectance measurements performed on the as-grown doped Ge-on-Si wafers (a typical TEM section is shown in **Figure 5**a) display a sharp plasma edge (fall-off of the reflectance) indicating the highest electromagnetic frequency at which free carriers can screen the radiation electric field,[47] which falls in the mid-IR (Figure 5b). The complex dielectric function $\varepsilon' + i\varepsilon''$ extracted by fitting the Drude model to the reflectance data[30] (Figure 5c,d) provides a direct measure of n through the determination of the zero-crossing point of ε', called the screened plasma frequency $\omega_p = \sqrt{ne^2/\varepsilon_\infty m^*}$, where e is the elementary charge, $m^* = 0.12 m_e$ is the conductivity effective mass, and $\varepsilon_\infty = 16$ is the dielectric screening constant of Ge. The high n, the small m^*, and the long mean free paths typical of crystalline n-Ge are all crucial to obtain functionalized tips with high ω_p in the mid-IR. Indeed, the TEM cross-section in Figure 5a shows no threading dislocations in most of the crystal structure of the n-Ge film, a feature obtained by the rapid stress-release at the first steps of the LEPECVD growth, indicating that there is no extrinsic contribution to electron scattering due to crystal defects.[30] The n-Ge pyramids attached to scanning probes can act as resonant plasmonic probes for s-SNOM at $\lambda \approx 10$ μm,[4] corresponding to the giant polarizability typically observed in plasmonic nanoparticles close to their ω_p.

Functionalized probe tips fabricated out of epitaxial Ge-on-Si with carrier density n = 2.5×10^{19} cm^{-3} resulting in a screened plasma frequency of $\omega_p = 1050$ cm^{-1} were employed for s-SNOM in the mid-IR (λ = 8–12 μm), using a commercial instrument enabling mid-IR nanospectroscopy of samples with a lateral resolution of few tens of nanometers.[39,48] The s-SNOM instrument consists of an AFM working in tapping mode where the probe tip is illuminated
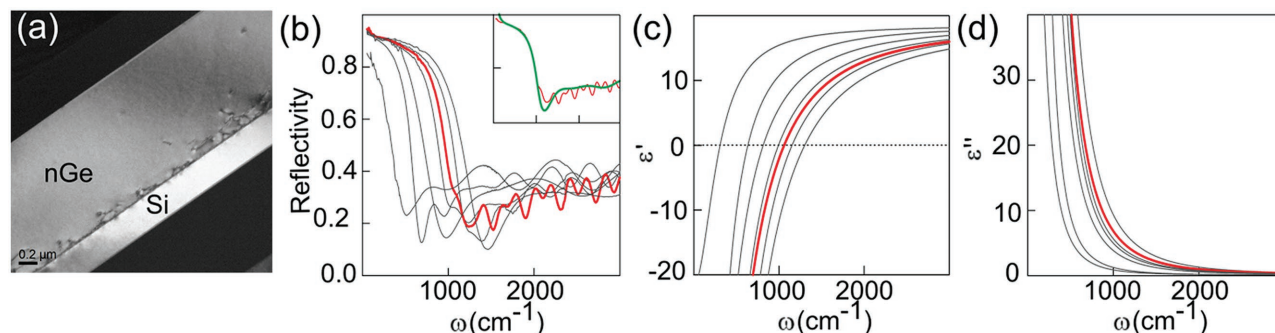

Figure 5. Mid-infrared characterization of the as-grown epitaxial material. a) TEM cross-view image of the type of Ge/Si heteroepitaxial layers used in this work: at the interface with Si (appearing white) one sees a strain-relaxation region of defected Ge material, followed by a relaxed electron-doped Ge layer (appearing light gray). b) IR normal-incidence reflectance spectra of different wafers of heavily electron-doped Ge-on-Si (from a minimum of $n = 0.35 \times 10^{19}$ cm^{-3} to a maximum of $n = 3.6 \times 10^{19}$ cm^{-3}). The steep edge is a signature of the highest frequency at which free carriers can screen the radiation electric field. The curve for the specific wafer used for the functionalization of the tips presented in this work is highlighted in red color. c,d) Real (ε') and imaginary (ε'') part of the n-Ge dielectric function calculated by Kramers–Kronig transformations applied to the reconstructed infinite-medium reflectivity (see the inset of panel (b)). The zero crossing of the real part in panel (c) indicates the value of ω_p.

at grazing incidence by a focused mid-IR laser beam. In s-SNOM, the component of the back-scattered radiation originating from the near-field tip–sample interaction is isolated and amplified by lock-in techniques in order to provide the user with information on the optical properties of the sample at the nanoscale.[49] A near-field scattering signal is expected when the tip approaches the sample surface and it is proportional to the polarizability of the coupled tip–sample system. The near-field signal is also expected to be significantly higher at a frequency ω_{IR} if free charge carriers are present in the tip, or in the sample, or in both, provided that the free carriers can screen the radiation electric field at ω_{IR} (i.e., if $\omega_{IR} < \omega_p$), insofar increasing the scattering cross-section of the tip–sample system. Experiments were performed with several functionalized tips and two different mid-IR lasers emitting at ω_{IR1} = 884 cm^{-1} (λ_{IR1} = 11.3 µm) and ω_{IR2} = 1250 cm^{-1} (λ_{IR2} = 8.0 µm), i.e., above and below ω_p = 1050 cm^{-1} (λ_p = 9.3 µm). The sample was an insulating Si substrate with a 1 µm thick heavily doped Ge film (n = 2.3 × 10^{19} cm^{-3}), which was locally etched down to the substrate to produce either conducting or insulating flat surfaces nearby. The near-field approach curves in **Figure 6**a were measured versus the tip–sample distance h during the approach of the probe tip to the sample surface. The fast rise for decreasing tip–sample distance ($h \rightarrow 0$) proves the near-field nature of this signal. By comparing the approach curves obtained on the same insulating sample surface at ω_{IR1} and at ω_{IR2} (blue and green curves, respectively), a clear suppression of the signal is seen at ω_{IR2}. The mid-IR frequency-dependent polarizability of a point-like dipole made out of the epitaxial Ge layers in Figure 6b, directly calculated from the dielectric function of Figure 5c,d, displays a higher value below ω_p. One can therefore reasonably ascribe the strong (weak) near-field signal observed at $\omega < \omega_p$ ($\omega > \omega_p$) to the frequency-dependent polarizability of the tip under the assumption that it is made of high-crystal quality epitaxial germanium and that its doping level of the epitaxial layers was unchanged during the functionalization process. Note that the amorphous surface layer shown in Figure 2 would not display such a clear frequency dependence of the polarizability. Finally, when testing the n-Ge tip at ω_{IR1} on the conducting sample surface (red curve in Figure 6a), a near-field signal even stronger than that of the blue curve is obtained, probably due to the polarizability maximum at similar frequencies in both the tip and the sample, which increases the strength of the tip–sample near-field interaction. Note that in this tip the polarizability maximum is achieved very close to the standard carbon dioxide laser wavelength of 10.6 µm, which represents one of the most efficient and low-cost laser systems and could then be used to build a compact and efficient version of s-SNOM employing the present tips.

The use of our functionalized tips as scanning probes for s-SNOM imaging has been finally demonstrated on a test sample consisting in doped semiconductor nanowires (ZnO) embedded in an elastomeric solid matrix (poly(dimethylsiloxane) (PDMS)), currently employed as the building blocks of nano-piezogenerators.[50] **Figure 7**a shows the AFM topography map of a sample region containing two neighboring nanowires embedded in the PDMS matrix obtained with one of the epitaxial Ge tips. The sample structure is better visualized in the FIB slice and view section of two neighboring nanowires in Figure 7b, where it
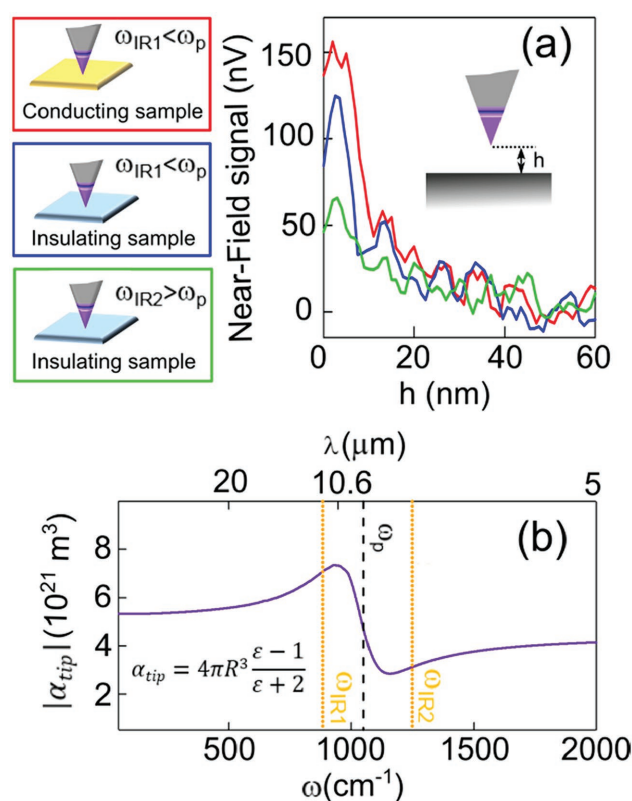
Figure 6. Scattering SNOM performed in the mid-IR with one n-Ge tip. a) Normalized near-field approach curves obtained on an insulating Si substrate at ω_{IR1} = 884 cm^{-1} (blue curve) and at ω_{IR2} = 1250 cm^{-1} (green curve), and on a conducting 1 µm thick film made of doped Ge at ω_{IR1} = 884 cm^{-1} (red curve). b) Absolute value of the n-Ge tip polarizability α_{tip} calculated using the formula of the polarizability for a sphere of radius R = 75 nm: $\alpha_{tip} = 4\pi R^3 (\varepsilon - 1)/(\varepsilon + 2)$ where ε is the complex dielectric function extracted from the IR characterization of the as-grown epitaxial layers (see Figure 5). The plasma frequency of the as-grown material ω_p and the s-SNOM laser frequencies, ω_{IR1}, ω_{IR2} are also indicated with vertical lines.

appears that they are actually buried below a conformal layer of PDMS. The electric conductivity of these devices is difficult to test by conducting-AFM or other nanoelectrical techniques, because of the unavoidable presence of the insulating matrix. Mid-IR spectroscopy is the technique of choice to characterize the local free carrier density in semiconductors,[51,52] however near-field mid-IR imaging is necessary in the case of nanowires, because both their individual size and mutual distance can be much smaller than the wavelengths that have to be used to sense the free carriers ($\lambda > 5$ µm). In Figure 7c it is reported the AFM topography line scan indicated by the dashed red line in Figure 7a, while in Figure 7d it is reported the corresponding profile of the s-SNOM signal acquired at ω_{IR1} = 884 cm^{-1}. At the nanowire positions, not precisely visible in the AFM topography profile due to the presence of the embedding matrix, sharp peaks appear instead in the s-SNOM profile, indicating the presence and the position of the nanowires themselves. The lateral resolution of the near-field profile $\Delta x \approx 100$ nm, derived from the data in Figure 7d, is deeply subwavelength ($\lambda = 11.3$ µm).

small
methods
www.small-methods.com

ADVANCED
SCIENCE NEWS
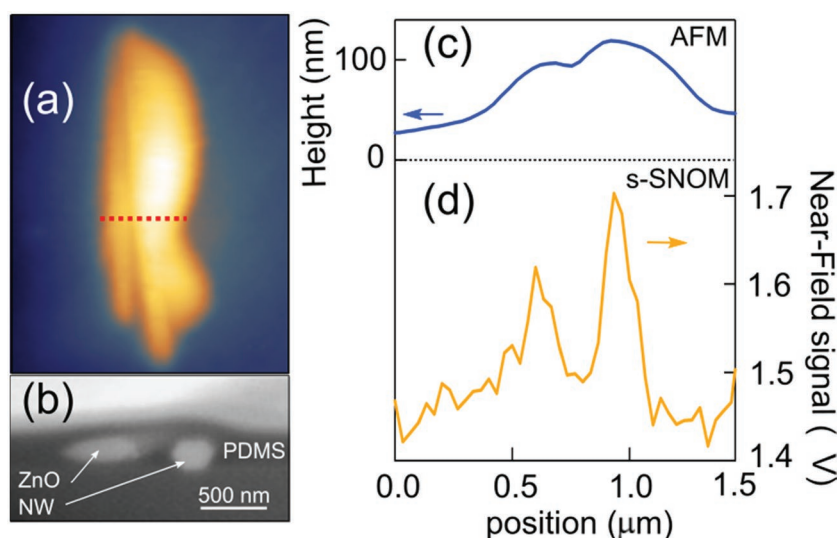www.advancedsciencenews.com

FULL PAPER

Figure 7. a) Topography map of the two adjacent nanowires embedded in PDMS obtained with an epitaxial n-Ge tip. b) FIB slice and view section of two neighboring nanowires on the same sample showing the embedding matrix material (dark gray), the nanowire sections (light gray polygons), and the support substrate. The white material on top is extrinsic to the sample, as it was deposited only before performing FIB slice and view. AFM topography profile c) taken along the line scan indicated by the dashed red line in panel (a) (blue curve, left axis) and the corresponding s-SNOM signal profile d) measured at $\omega_{IR1} = 884$ cm^{-1} (orange curve, right axis).

5. Conclusion

The functionalization of scanning probe tips with epitaxial materials has been presented and the structural properties, chemical composition, and optical functions of the tips have been studied. The nanotechnology method is based on the transfer of the epitaxial layers from the growth substrate to a silicon cantilever and on the subsequent shaping of the transferred layers into a pyramidal tip by focused ion beam. Scanning probe tips have been functionalized with electron-doped germanium layers grown on silicon wafers by plasma-enhanced chemical vapor deposition. Nanoscale structural characterization has revealed that the pyramidal tips retained the high crystal quality typical of the epitaxial semiconductor growth, and elemental composition mapping has shown that they were not significantly contaminated by etching and milling agents during the functionalization process. Two different nano-optics experiments were performed: photoluminescence emission by a nanoscale probe tip at the standard telecom wavelengths of 1.55 µm in the near-infrared, and scattering scanning near-field optical microscopy around the standard carbon dioxide laser wavelength of 10.6 µm in the mid-infrared. While demonstrating potential applications, the performed nano-optics experiments also show that the optical properties of the as-grown epitaxial material are preserved in the functionalized scanning probe tips.

The presented technology can be potentially employed to functionalize tips with other epitaxial materials, independently from the substrate type used for the epitaxial growth. The present choice of germanium-on-silicon films grown by low-energy plasma-enhanced chemical vapor deposition, however, is compatible with future up-scaled production of silicon cantilevers with functionalized tips, which can be achieved by

suitable modification of parallel lithographic fabrication processes of scanning probes for microscopy.

6. Experimental Section

Tip Fabrication: The tip fabrication technique is based on the combination of three mainstream nanofabrication technologies: deep reactive ion etching (deep-RIE), FIB, and EB-ID. Starting from commercial silicon scanning probe chips (visible-apex Nanosensor AdTEC) with cantilever length and stiffness suitable for the final application (either contact or noncontact mode), a number of them were prepared for functionalization by cutting out the existing AFM tip apex by FIB milling, hence producing a flat-top surface of around 1 µm^2 at the probe end. The Ge-on-Si epitaxial wafers were patterned into micropillar fields by lithography, using a deep-RIE recipe based on sulfur hexafluoride and inductively coupled plasma that produces vertical walls. Micropillars on the same wafer had different section (circular, triangular, squared) and size (1–3 µm side) according to different tip designs. The patterned wafers were inserted in the vacuum chamber of a dual-beam apparatus with both FIB milling and EB-ID capabilities (Zeiss Auriga Xbeam). By using a piezoelectric nanomanipulator and a 5-axis positioner to remotely operate in the chamber, the flat-top modified AFM probe was put in surface contact with the top of one selected micropillar. At this point, EB-ID of a platinum–carbon alloy was performed to glue the probe to the pillar, and subsequently the base of the pillar was cut by FIB milling, the pillar, glued to the silicon cantilever, was lifted out of the wafer. The cantilever chip was then mounted on a manipulator and reinserted in the FIB chamber, where fine milling at low ion currents (1 pA) was performed to obtain the desired tip geometry, with 3D accuracy around 25 nm. The procedure was repeated for each functionalized tip. Four-side pyramids with different apical angle and curvature radius of 50–100 nm were sculptured, but different designs are certainly possible. The functionalized probes can now be used as standard silicon cantilever probes in any AFM setup with no further adaptation.

Transmission Electron Microscopy: TEM analysis was performed with a 2100-F JEOL electron microscope operated at an acceleration voltage of 200 kV and equipped with an Oxford INCA X-ray energy-dispersive spectrometer.

Photoluminescence Microscopy: PL spectra and spatial maps of the spontaneous emission of n-Ge tip were obtained with a confocal reflection microscope. The germanium tip was mounted on a sample holder placed on a XYZ piezo stage (P-517.3CL, Physik Instrumente) for scanning. A solid-state laser emitting at $\lambda = 785$ nm was focused on the tip apex via a 0.9 NA objective which also collects back the emitted photoluminescence. The collected emission, passing through a 50:50 infrared-coated beam splitter was filtered to reject the excitation light using a set of long-pass filters with cutoff wavelength around 1300 nm. The filtered emission was sent into a home-made spectrometer,[38] working in the 800–1700 nm spectral region, equipped with a InGaAs/InP single-photon avalanche photodetector (SPAD) that operates in gated-mode,[53] and a rotating dispersion prism (Pelin–Broca Prism). The spectral resolution is about $\Delta\lambda = 15$ nm. The setup is also used to acquire spatial maps of the PL emission by selecting a specific spectral window while scanning the piezo stage.

Scattering Scanning Near-Field Microscopy: The mid-IR near-field microscopy experiment was performed by using a commercial apertureless scattering-type SNOM (NeaSNOM by Neaspec GmbH). This platform combines AFM with optical imaging and spectroscopy at

ADVANCED
SCIENCE NEWS
www.advancedsciencenews.com

small
methods
www.small-methods.com

the nanoscale by coupling an AFM system with mid-IR lasers. Because of the optical near-field interaction between the tip and the sample, the backscattered light contains information about the local dielectric function of the sample, including information on the free carrier density. In the s-SNOM system, the light scattered by the tip was collected by a parabolic mirror and the topography map was simultaneously recorded, so as to associate each pixel of the scattered intensity map to a pixel in the topography map. Mid-IR s-SNOM experiments were performed with a tunable CO_2 laser operating at $\lambda = 11.3$ µm ($\omega_{IR1} = 884$ cm^{-1}) and with a quantum cascade laser operating at $\lambda = 8.0$ µm ($\omega_{IR2} = 1250$ cm^{-1}). The incident radiation was transverse-magnetic (TM)-polarized with an angle of incidence of 70°. Background contributions, which do not contain information about the near-field interaction between the tip and the sample, were suppressed by vertical oscillation of the tip at a tapping frequency Ω and collecting the detector signal demodulated at the higher harmonics 2Ω, 3Ω. In Figure 6a and 7d, the s-SNOM signal was obtained demodulating the detector signal at the second and third harmonic of the tapping frequency, respectively. The signal intensity at ω_{IR2} was normalized to that at ω_{IR1} by taking into account the measured laser power and detector responsivity, and the Rayleigh factor proportional to ω^4.

Acknowledgements

[1] P. J. Schuck, A. Weber-Bargioni, P. D. Ashby, D. F. Ogletree, A. Schwartzberg, S. Cabrini, *Adv. Funct. Mater.* **2013**, *23*, 2539.

[2] W. Bao, M. Melli, N. Caselli, F. Riboli, D. S. Wiersma, M. Staffaroni, H. Choo, D. F. Ogletree, S. Aloni, J. Bokor, S. Cabrini, F. Intonti, M. B. Salmeron, E. Yablonovitch, P. J. Schuck, A. Weber-Bargioni, *Science* **2012**, *338*, 1317.

[3] K. F. Domke, B. Pettinger, *ChemPhysChem* **2010**, *11*, 1365.

[4] F. Huth, A. Chuvilin, M. Schnell, I. Amenabar, R. Krutokhvostov, S. Lopatin, R. Hillenbrand, *Nano Lett.* **2013**, *13*, 1065.

[5] M. Celebrano, P. Biagioni, M. Zavelani-Rossi, D. Polli, M. Labardi, M. Allegrini, M. Finazzi, L. Du, G. Cerullo, *Rev. Sci. Instrum.* **2009**, *80*, 033704.

[6] A. Lewis, K. Lieberman, *Nature* **1991**, *354*, 214.

[7] M. Frimmer, Y. Chen, A. F. Koenderink, *Phys. Rev. Lett.* **2011**, *107*, 123602.

[8] Y. Zhang, P. S. Dobson, J. M. R. Weaver, *Microelectron. Eng.* **2011**, *88*, 2435.

[9] S. V Kalinin, N. Balke, *Adv. Mater.* **2010**, *22*, E193.

[10] D. P. Burt, N. R. Wilson, J. M. R. Weaver, P. S. Dobson, J. V. Macpherson, *Nano Lett.* **2005**, *5*, 639.

[11] W. Smirnov, A. Kriele, R. E. Hoffmann, E. Sillero, J. Hees, O. A. Williams, N. Yang, C. Kranz, C. E. Nebel, *Anal. Chem.* **2011**, *83*, 4936.

[12] T. W. Johnson, Z. J. Lapin, R. Beams, N. C. Lindquist, S. G. Rodrigo, L. Novotny, S. H. Oh, *ACS Nano* **2012**, *6*, 9168.

[13] M. A. Lantz, B. Gotsmann, P. Jaroenapibal, T. D. B. Jacobs, S. D. O'Connor, K. Sridharan, R. W. Carpick, *Adv. Funct. Mater.* **2012**, *22*, 1639.

[14] R. D. Piner, *Science* **1999**, *283*, 661.

[15] J. D. Torrey, S. E. Vasko, A. Kapetanovic, Z. Zhu, A. Scholl, M. Rolandi, *Adv. Mater.* **2010**, *22*, 4639.

[16] N. Chevalier, M. J. Nasse, J. C. Woehl, P. Reiss, J. Bleuse, F. Chandezon, S. Huant, *Nanotechnology* **2005**, *16*, 613.

[17] Y. Ebenstein, T. Mokari, U. Banin, *J. Phys. Chem. B* **2004**, *108*, 93.

[18] J. Fulmes, R. Jäger, A. Bräuer, C. Schäfer, S. Jäger, D. A. Gollmer, A. Horrer, E. Nadler, T. Chassé, D. Zhang, A. J. Meixner, D. P. Kern, M. Fleischer, *Nanoscale* **2015**, *7*, 14691.

[19] M. Motoyama, F. B. Prinz, *ACS Nano* **2014**, *8*, 3556.

[20] G. M. Cohen, H. F. Hamann, US Patent *US 7.572.300 B2*, **2009**.

[21] Q. Ye, A. M. Cassell, H. Liu, K. J. Chao, J. Han, M. Meyyappan, *Nano Lett.* **2004**, *4*, 1301.

[22] L. Aigouy, M. Mortier, J. Gírak, E. Bourhis, Y. De Wilde, P. Corstjens, H. J. Tanke, *J. Appl. Phys.* **2005**, *97*, 104322.

[23] P. Schon, J. Geerlings, N. Tas, E. Sarajlic, *Anal. Chem.* **2013**, *85*, 8937.

[24] C. Ropers, C. C. Neacsu, T. Elsaesser, M. Albrechty, M. B. Raschke, C. Lienau, *Nano Lett.* **2007**, *7*, 2784.

[25] F. De Angelis, G. Das, P. Candeloro, M. Patrini, M. Galli, A. Bek, M. Lazzarino, I. Maksymov, C. Liberale, L. C. Andreani, E. Di Fabrizio, *Nat. Nanotechnol.* **2010**, *5*, 67.

[26] L. Novotny, N. van Hulst, *Nat. Photonics* **2011**, *5*, 83.

[27] M. Fleischer, A. Weber-Bargioni, M. V. P. Altoe, A. M. Schwartzberg, P. J. Schuck, S. Cabrini, D. P. Kern, *ACS Nano* **2011**, *5*, 2570.

[28] C. Kranz, G. Friedbacher, B. Mizaikofft, A. Lugstein, J. Smoliner, E. Bertagnolli, *Anal. Chem.* **2001**, *73*, 2491.

[29] M. Fleischer, *Nanotechnol. Rev.* **2012**, *1*, 313.

[30] J. Frigerio, A. Ballabio, G. Isella, E. Sakat, P. Biagioni, M. Bollani, E. Napolitani, C. Manganelli, M. Virgilio, A. Grupp, M. P. Fischer, D. Brida, K. Gallacher, D. J. Paul, L. Baldassarre, P. Calvani, V. Giliberti, A. Nucara, M. Ortolani, *Phys. Rev. B* **2016**, *94*, 085202.

[31] H. Rosenblad, C. Deller, H. R. Dommann, A. Meyer, T. Schroeter, P. Von Känel, *J. Vac. Sci. Technol. A* **1998**, *16*, 2785.

[32] D. J. Paul, *Adv. Mater.* **1999**, *11*, 191.

[33] K. A. McComber, X. Duan, J. Liu, J. Michel, L. C. Kimerling, *Adv. Funct. Mater.* **2012**, *22*, 1049.

[34] M. Bollani, D. Chrastina, A. Fedorov, R. Sordan, A. Picco, E. Bonera, *Nanotechnology* **2010**, *21*, 475302.

[35] H. Von Känel, D. Chrastina, B. Rössner, G. Isella, J. P. Hague, M. Bollani, *Microelectron. Eng.* **2004**, *76*, 279.

[36] J. Frigerio, M. Lodari, D. Chrastina, V. Mondiali, G. Isella, M. Bollani, *J. Appl. Phys.* **2014**, *116*, 113507.

[37] V. Giliberti, E. Sakat, L. Baldassarre, A. Di Gaspare, A. Notargiacomo, E. Giovine, J. Frigerio, G. Isella, M. Melli, A. Weber-Bargioni, S. Aloni, S. Sassolini, S. Cabrini, P. Biagioni, M. Ortolani, M. Bollani, *Microelectron. Eng.* **2015**, *141*, 168.

[38] M. Celebrano, M. Baselli, M. Bollani, J. Frigerio, A. Bahgat Shehata, A. Della Frera, A. Tosi, A. Farina, F. Pezzoli, J. Osmond, X. Wu, B. Hecht, R. Sordan, D. Chrastina, G. Isella, L. Duò, M. Finazzi, P. Biagioni, *ACS Photonics* **2015**, *2*, 53.

[39] F. Keilmann, R. Hillenbrand, *Philos. Trans. R. Soc. A* **2004**, *362*, 787.

[40] R. Soref, *Nat. Photonics* **2010**, *4*, 495.

[41] J. Michel, J. Liu, L. C. Kimerling, *Nat. Photonics* **2010**, *4*, 527.

[42] S. Wirths, R. Geiger, N. von den Driesch, G. Mussler, T. Stoica, S. Mantl, Z. Ikonic, M. Luysberg, S. Chiussi, J. M. Hartmann, H. Sigg, J. Faist, D. Buca, D. Grützmacher, *Nat. Photonics* **2015**, *9*, 88.

small
methods
www.small-methods.com

**ADVANCED
SCIENCE NEWS**
www.advancedsciencenews.com

FULL PAPER

[43] J. Liu, X. Sun, R. Camacho-Aguilera, L. C. Kimerling, J. Michel, *Opt. Lett.* **2010**, *35*, 679.

[44] P. H. Lim, S. Park, Y. Ishikawa, K. Wada, *Opt. Express* **2009**, *17*, 16358.

[45] M. Bollani, V. Giliberti, E. Sakat, L. Baldassarre, M. Celebrano, J. Frigerio, G. Isella, M. Finazzi, M. Melli, A. Weber-Bargioni, S. Cabrini, P. Biagioni, M. Ortolani, *Microelectron. Eng.* **2016**, *159*, 164.

[46] S. A. Maier, M. L. Brongersma, P. G. Kik, S. Meltzer, A. A. G. Requicha, H. A. Atwater, *Adv. Mater.* **2001**, *13*, 1501.

[47] L. Baldassarre, E. Sakat, J. Frigerio, A. Samarelli, K. Gallacher, E. Calandrini, G. Isella, D. J. Paul, M. Ortolani, P. Biagioni, *Nano Lett.* **2015**, *15*, 7225.

[48] F. Huth, A. Govyadinov, S. Amarie, W. Nuansing, F. Keilmann, R. Hillenbrand, *Nano Lett.* **2012**, *12*, 3973.

[49] R. Hillenbrand, B. Knoll, F. Keilmann, *J. Microsc.* **2001**, *202*, 77.

[50] Z. L. Wang, J. Song, *Science* **2006**, *312*, 242.

[51] A. J. Huber, F. Keilmann, J. Wittborn, J. Aizpurua, R. Hillenbrand, *Nano Lett.* **2008**, *8*, 3766.

[52] J. M. Stiegler, A. J. Huber, S. L. Diedenhofen, J. Gómez Rivas, R. E. Algra, E. P. A. M. Bakkers, R. Hillenbrand, *Nano Lett.* **2010**, *10*, 1387.

[53] M. A. Itzler, X. Jiang, M. Entwistle, K. Slomkowski, A. Tosi, F. Acerbi, F. Zappa, S. Cova, *J. Mod. Opt.* **2011**, *58*, 174.